China Ocean Eng., 2021, Vol. 35, No. 5, P. 712–723
DOI: https://doi.org/10.1007/s13344-021-0063-7, ISSN 0890-5487
http://www.chinaoceanengin.cn/ E-mail: coe@nhri.cn

Harmonic Analyses of Hydrodynamic Characteristics for Gap Resonance Between Fixed Box and Vertical Wall

HE Zhi-wei[a], GAO Jun-liang[a, *], CHEN Hong-zhou[b], ZANG Jun[c], LIU Qian[a], WANG Gang[d]

[a] School of Naval Architecture and Ocean Engineering, Jiangsu University of Science and Technology, Zhenjiang 212100, China

[b] School of Civil Engineering and Architecture, Northeast Electric Power University, Jilin 132012, China

[c] Centre for Infrastructure, Geotechnical and Water Engineering (IGWE), Department of Architecture and Civil Engineering, University of Bath, BA2 7AY, UK

[d] College of Harbour, Coastal and Offshore Engineering, Hohai University, Nanjing 210098, China

Received January 25, 2021; revised August 23, 2021; accepted September 14, 2021

Abstract

Two marine structures arranged side by side with a narrow gap may suffer from violent free-surface resonance, which would cause green water on deck, dramatically raise hydrodynamic loads on structures and seriously threaten the operation safety. The CFD-based open-sourced software, OpenFOAM®, is employed to simulate the two-dimensional fluid resonance inside a narrow gap between a fixed box and a vertical wall induced by regular waves with different wave heights. The topographies with various plane slopes are placed in front of the wall. The focus of this article is on the influences of the incident wave height and the topographic slope on the nonlinear characteristics of various hydrodynamic parameters (including the wave height in the gap, the vertical wave force, and the horizontal wave force on the box) during gap resonance. The ratios of their high-order to the corresponding 1st-order components under different sets of the incident wave height and the topographic slope are analyzed. It is found that the relative importance of all the high-order components increases gradually with the incident wave height for all the three parameters. The topographic influence on them closely depends on the type of the parameters and the incident wave height. In addition, the occurrence of the 2nd-order gap resonance phenomenon can cause the 2nd-order wave height and horizontal force to be significantly larger than the corresponding 1st-order components.

Key words: gap resonance, harmonic analyses, resonant wave height, wave loads, OpenFOAM®

Citation: He, Z. W., Gao, J. L., Chen, H. Z., Zang, J., Liu, Q., Wang, G., 2021. Harmonic analyses of hydrodynamic characteristics for gap resonance between fixed box and vertical wall. China Ocean Eng., 35(5): 712–723, doi: https://doi.org/10.1007/s13344-021-0063-7

1 Introduction

Two marine structures arranged side by side with a narrow gap between them are frequently utilized in the field of ocean engineering. A typical example of such structure layout is the Liquefied Natural Gas Carriers (LNGC) and Floating Production Storage and Offloading (FSPO) units. They are often deployed side by side with a narrow gap between them as the liquefied natural gas production is conveyed from the FSPO unit to the LNGC (Zhao et al., 2018). Under conditions of specific wave frequencies, a violent free-surface motion may occur in the gap, and this kind of phenomenon is often called "*gap resonance*". It can result in the green water on the deck (Gao et al., 2020a; Zhao et al., 2018) and dramatically increase the hydrodynamic loads acting on the structure when compared with the same isolated structure (Miao et al., 2000). The safety of both the structure and the engineering operation would be seriously threatened.

The methodologies adopted in the research of gap resonance include analytical, experimental, and numerical analyses/simulations. The analytical analyses that were employed in the early stage of the related studies were basically based on the linear potential flow theory (e.g., Miao et al., 2001; Molin et al., 2002). Subsequently, numerous laboratory experiments were implemented to verify the previous analytical investigations, and the real understanding of

Foundation item: This research is financially supported by the National Key Research and Development Program of China (Grant No. 2017YFC1404200), the National Natural Science Foundation of China (Grant Nos. 51911530205 and 51809039), the Natural Science Foundation of Jiangsu Province (Grant Nos. BK20201455 and BK20210885), the Natural Science Foundation of the Jiangsu Higher Education Institutions (Grant No. 20KJD170005) and the Qing Lan Project of Jiangsu Universities. The work is also partially supported by UK EPSRC (Grant No. EP/T026782/1), the Royal Academy of Engineering (Grant No. UK-CIAPP/73) and the Royal Society (Grant No. IEC\NSFC\181321).

*Corresponding author. E-mail: gaojunliang880917@163.com

the phenomenon was further enhanced. Saitoh et al. (2006) carried out two-dimensional (2D) experiments in a wave flume to study the gap resonance inside a narrow gap between two fixed structures. A series of 2D tests were further performed by Tan et al. (2014) to investigate the gap resonance occurring inside a gap between a fixed box and a vertical wall. Recently, to gain more insights into the three-dimensional (3D) fluid resonance between two barges or between FSPO and LNGC, some 3D physical experiments were implemented by Zhao et al. (2017).

Most of the numerical investigations so far utilized the classic potential flow theory combined with various numerical techniques, such as the scaled boundary finite element method or the boundary element method (Li et al., 2005; Tan et al., 2020). However, they were reported to overestimate the resonant wave height and the wave loads because the wave energy dissipation due to the fluid viscosity cannot be considered in the context of the potential flow model. To overcome this shortcoming, several numerical methods that can artificially introduce the wave energy dissipation into the potential flow model have been proposed (e.g., Liu et al. (2020); Tan et al. (2019)). Comparisons of numerical results and experimental data have illustrated that the potential flow model with these corrections may perform well on the gap resonance problem.

In the last decade, the Computational Fluid Dynamics (CFD) based numerical model has become an effective tool in the research of gap resonance. Lu et al. (2011) employed a Navier−Stokes equation model to investigate the features of the resonant motions of the fluid inside narrow gaps between multiple boxes. Subsequently, based on an open-source CFD package OpenFOAM®, Moradi et al. (2015) studied the effects of the inlet configurations on the 2D free surface oscillation in the narrow gap. Jiang et al. (2019) studied the fluid resonance between two non-identical boxes and the wave loads on the boxes. Similarly, based on OpenFOAM®, the gap resonance between the ship cross-section and the vertical quay was investigated in Gao et al. (2019a, 2020b) and Lu et al. (2020). Recently, Gao et al. (2021a) and He et al. (2021) studied the influences of the motion of the upstream box on the hydrodynamic behavior of the resonant fluid inside the gap between two side-by-side boxes and on the wave forces acting on both boxes, respectively. Based on OpenFOAM®, some efforts on the 3D gap resonance problem were also carried out by Wang et al. (2019).

Although many studies on gap resonance were carried out, attention has been basically focused on the analyses of the total resonant wave height inside the gap between multiple structures and the total wave loads acting on the structure (Gao et al., 2019a; Lu et al., 2011; Ning et al., 2018). Numerous investigations have shown that the nonlinearity of waves and/or wave loads plays an important role in many physical phenomena (e.g., Chen et al., 2018; Gao et al., 2020c, 2019d, 2021c ; Grue and Huseby, 2002). However, the studies on the nonlinear hydrodynamic characteristics of gap resonance are relatively few. Based on two different 3D time-domain potential flow models, Sun et al. (2010) performed the 1st- and the 2nd-order analysis of the resonant free surface inside the gap between two adjacent barges in close proximity. By employing a 2D fully nonlinear potential flow computer program, Li (2019) studied the 2nd-order effects of wave elevations and hydrodynamic forces during the 2nd-order gap resonance between two floating bodies. Based on OpenFOAM®, Gao et al. (2019c) performed the harmonic analyses of the free-surface elevation in a narrow gap between two fixed boxes and wave loads on the boxes. It can be seen from the above literature that the limited nonlinear hydrodynamic analyses focused only on the gap resonance problem between two floating/fixed bodies.

Recently, considering that real harbors generally have uneven bottoms and the local topography in front of the quay is usually variable (e.g., Gao et al., 2019b, 2021b), the influences of both the incident wave height and the topographic variation on the total resonant wave heights between a ship cross-section and a vertical quay and on the total wave loads on the ship cross-section were systematically investigated by Gao et al. (2019a, 2020b). However, the nonlinear features of these hydrodynamic parameters under conditions of various incident wave heights and topographies are still unknown. This is the primary motivation of the current study.

This article is a direct extension of the studies of the above two papers. Based on a series of numerical simulations in a 2D numerical wave tank, the effects of both the incident wave height and the topographic slope on the relative importance of the high-order (including the 2nd- and the 3rd-order) components to the 1st-order ones for various hydrodynamic parameters during gap resonance will be investigated comprehensively. The hydrodynamic parameters considered include the wave height in the gap, the vertical wave force, and the horizontal wave force on the ship cross-section. However, compared with Gao et al. (2019a, 2020b), the lower limit of the incident wave frequency considered in this paper is extended to a much smaller value so that the possible 2nd-order gap resonance phenomenon may occur in the present study.

This paper is organized as follows. Section 2 briefly introduces the numerical model utilized. Section 3 describes the setups of the numerical wave tank. Then, analysis results and related discussions are presented in Section 4. Finally, conclusions are drawn in Section 5.

2 Numerical model description

To accurately simulate the wave energy dissipation around the gap caused by the fluid viscosity, a CFD-based flow solver is essential. The present study is based on the OpenFOAM® two-phase solver "*interFoam*" with the incor-

poration of the "*waves2Foam*" toolbox for producing and dissipating waves (Jacobsen et al., 2012).

The continuity equation

$$\frac{\partial \rho}{\partial t}+\nabla\cdot(\rho \boldsymbol{u})=0 \tag{1}$$

and the Navier−Stokes equations

$$\frac{\partial \rho \boldsymbol{u}}{\partial t}+\nabla\cdot\left(\rho \boldsymbol{u}\boldsymbol{u}^{\mathrm{T}}\right)=-\nabla p-(\boldsymbol{g}\cdot\boldsymbol{x})\nabla\rho+\nabla\cdot(\mu\nabla\boldsymbol{u})+\sigma_{\mathrm{t}}k_{\gamma}\nabla\gamma \tag{2}$$

are used to simulate the flow of air and water. In the above equations, t denotes time, $\nabla=(\partial/\partial x,\partial/\partial y,\partial/\partial z)$ denotes the spatial gradient, $\rho=\rho(\boldsymbol{x})$ denotes the fluid density, $\boldsymbol{u}$=(u, v, w) is the fluid velocity, p is the hydrodynamic pressure, $\boldsymbol{g}$ is the acceleration due to gravity, $\boldsymbol{x}$=(x, y, z) is the Cartesian coordinate, μ is the dynamic viscosity, and σ_{t}, k_{γ} and γ respectively denote the surface tension coefficient, the surface curvature and the volume fraction of water in a computational cell. The mixed fluid is captured by using γ that has a value of 0 for air and 1 for water and intermediate values for a mixture of air and water.

The scalar field γ is predicted by the following equation:

$$\frac{\partial \gamma}{\partial t}+\nabla\cdot(\gamma\boldsymbol{u})+\nabla\cdot[\gamma(1-\gamma)\boldsymbol{u}_{\mathrm{r}}]=0, \tag{3}$$

where $\boldsymbol{u}_{\mathrm{r}}=\boldsymbol{u}_{\mathrm{water}}-\boldsymbol{u}_{\mathrm{air}}$ denotes the relative fluid velocity between water and air. The detailed descriptions for the implementation of the above equation can be found in Berberović et al. (2009). By utilizing γ, any fluid property ψ (e.g., ρ and μ) can be calculated via a weighting function:

$$\psi=(1-\gamma)\psi_{\mathrm{air}}+\gamma\psi_{\mathrm{water}}, \tag{4}$$

where the subscripts "air" and "water" represent the corresponding fluid properties.

To produce desired incident regular wave trains, the velocity and the pressure gradient at the wave inlet boundary are set to the velocity of the regular waves and zero, respectively (see Fig. 1). At the upper boundary of the computational domain, the boundary condition is defined as the "atmosphere"; at its lower and right boundaries and at the solid walls of the fixed box, the "no-slip" condition is used. For a 2D simulation, the "empty" condition is applied on the walls in the third dimension.

A relaxation zone is placed around the wave inlet boundary to dissipate the reflected wave energy from the box-wall system. The exponential relaxation function

$$\alpha_{\mathrm{R}}(\chi_{\mathrm{R}})=1-\frac{\exp\left(\chi_{\mathrm{R}}^{3.5}\right)}{\exp(1)-1}\quad \text{for } \chi_{\mathrm{R}}\in[0,1] \tag{5}$$

is applied inside the relaxation zone in the following way:

$$\phi=\alpha_{\mathrm{R}}\phi_{\mathrm{computed}}+(1-\alpha_{\mathrm{R}})\phi_{\mathrm{target}}, \tag{6}$$

where ϕ represents either velocity (u) or volume of fraction of water/air (γ). The definition of χ_{R} is such that α_{R} is always 1 at the interface between the non-relaxed part of the computational domain and the relaxation zone. The subscripts "computed" and "target" for velocity represent the velocities that calculated in the computational domain and that evaluated or assigned from the chosen wave model, respectively.

Eqs. (1)−(3) are solved based on the finite volume method. The time derivatives are discretized by a 1st-order Euler scheme. The velocity-pressure coupling is resolved by employing the Pressure Implicit with Splitting of Operator (PISO) algorithm. To obtain accurate and stable numerical results, the maximum Courant number in all simulations is set to 0.25.

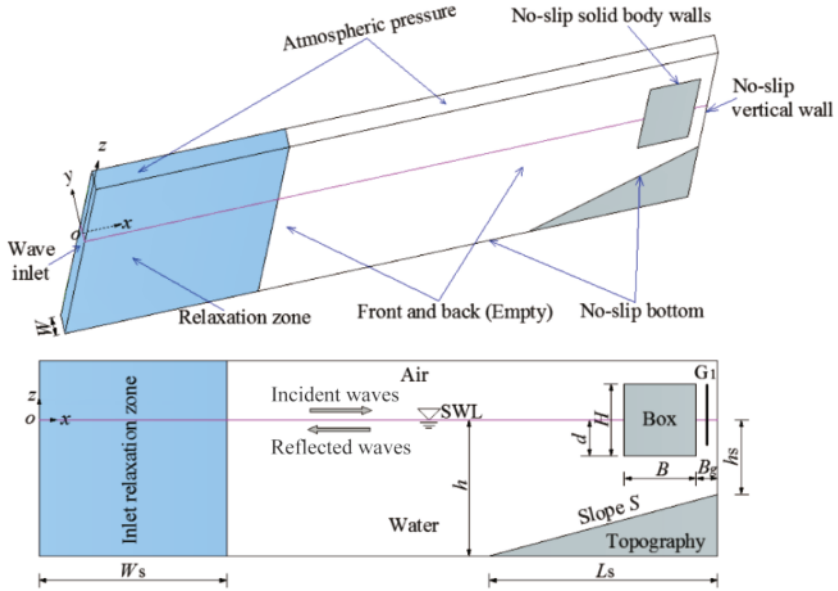

Fig. 1. Definition sketch of the numerical wave tank (NWT): the boundary conditions and the coordinate system (upper panel), and position of the wave gauge and definitions of geometric parameters (lower panel).

3 Numerical wave tank

The numerical wave tank (NWT) adopted is shown in Fig. 1. The height, the length, and the thickness (denoted by W) of the NWT are set to 0.8 m, 14.0 m, and 0.1 m, respectively, and its thickness corresponds to one computational cell. A fixed square-shaped box is used to represent the ship cross-section and is arranged very close to a fully reflective vertical wall. Both the height H and the breadth B of the box are 0.5 m, and the draft d = 0.25 m. The width of the narrow gap between the box and the wall is set to B_g = 0.05 m. The air depth, h_a, in all cases is a constant of 0.3 m. In the region of 12.0 < x < 14.0 m, the topography with various plane slopes exists below the box, and the horizontal length of the topography L_s = 2.0 m. The water depth in the deeper region, h, is a constant of 0.5 m, and the water depth in front of the vertical wall, h_s, is set to 0.50 m, 0.45 m, 0.40 m, 0.35 m, 0.30 m and 0.27 m. Correspondingly, the plane slopes, S, are equal to 0, 0.025, 0.050, 0.075, 0.100 and 0.113.

In Gao et al. (2019a, 2020b), the incident wave frequency, ω_I, varies from 2.514 rad/s to 5.586 rad/s. At the range of the frequency, only the 1st-order gap resonance phenomenon can be triggered. In this paper, to consider the possible 2nd-order gap resonance phenomenon that the fluid resonance inside the gap is excited by the 2nd-order harmonic component of the incident low-frequency waves (Li, 2019; Zhao et al., 2017), the lower limit of ω_I decreases further to 1.152 rad/s; while its upper limit remains the same as that in Gao et al. (2019a, 2020b). Five incident wave heights (i.e., H_0=0.005 m, 0.024 m, 0.050 m, 0.075 m, and 0.100 m) are considered here. The incident regular waves with various frequencies and wave heights are produced at the wave inlet boundary of the NWT according to the 2nd-order Stokes wave theory.

One wave gauge, G_1, is arranged in the middle of the gap to record the time series of free surface elevations therein. The width of the relaxation zone, W_s, varies from 8.0 m to 12.0 m to ensure that W_s is always larger than one incident wavelength in each case, which guarantees the effectiveness for dissipating the reflected wave energy (Jacobsen et al., 2012). As the largest flow velocity appears in the gap at resonance, the Reynolds number is defined as (Lu et al., 2020):

$$Re = \frac{V_g B_g}{\nu}, \tag{7}$$

where V_g is the amplitude of the oscillating velocity in the gap and $\nu = 1\times10^{-6}$ m^2/s is the kinetic viscosity of the water. In the present study, the maximum Re is approximately 5.24×10^4. Jensen et al. (1989) suggested that the laminar-to-turbulent transition would first occur at $Re \approx 10^5$ for oscillatory flow over a smooth plane wall. Hence, only the laminar flow model is utilized in the numerical model for the present study. Detailed descriptions on both the method of the mesh generation and the convergence analysis of the numerical result to the mesh resolution have been presented in Gao et al. (2020b), and they are not repeated here because of limited space.

Each of the cases runs for 40 s in total. It has been found from Gao et al. (2019a, 2020b) that the time series of both the wave elevation inside the gap and wave loads on the box have reached a steady state at 20 s. In the present study, the harmonic analyses are performed based on the discrete Fourier transform for their time series:

$$\varphi^{(m)} = \frac{1}{NT}\int_{t_0}^{t_0+NT} \varphi(t) e^{im\omega t} dt, \tag{8}$$

where $\varphi(t)$ is the time series of wave elevation or wave force, $\varphi^{(m)}$ is the corresponding amplitude of the m-th order harmonic component, i is the imaginary unit, and $T = 2\pi/\omega$ is the incident wave period. All the analysis results that will be shown in Section 4 are based on the steady-state free-surface elevations inside the gap and the steady-state wave loads on the box ranging from t_0=20 s to a maximum moment that equates to t_0+NT. N denotes a maximum integral which ensures the maximum moment is less than 40 s. Because the incident wave period varies from case to case, both the value of N and the maximum moment are not fixed in all cases.

4 Numerical results and discussion

In this section, the topics on how the variations of both the incident wave height and the topographic slope affect the 1st three order components of the wave height inside the gap and the wave loads are further studied. To facilitate the understanding of the research results in this paper, the variations of the total wave height and the total wave loads with respect to the incident wave frequency under a certain set of incident wave height and topographic slope are first presented in Subsection 4.1. Then, the results of the harmonic analyses on the wave height inside the gap, the vertical wave force, and the horizontal wave force are illustrated in Subsections 4.2−4.4, respectively. Finally, the comparisons of the harmonic analysis results for the above three parameters are presented in Subsection 4.5.

4.1 Total wave height inside the gap and total wave loads on the box

To facilitate readers' understanding of this paper, the variations of the total wave height inside the gap and the total wave forces on the box with respect to the incident wave frequency under conditions of H_0=0.024 m and S=0.050 are shown again in Fig. 2, where H_g, F_z, and F_x denote the total wave height inside the gap, the total vertical wave force, and the total horizontal wave force, respectively. It can be seen that for each of the three parameters, there always exists a maximum point at a specific wave frequency. In Fig. 2a, the wave frequency that corresponds to the maximum wave height inside the gap, ω_{Hg}, is referred to

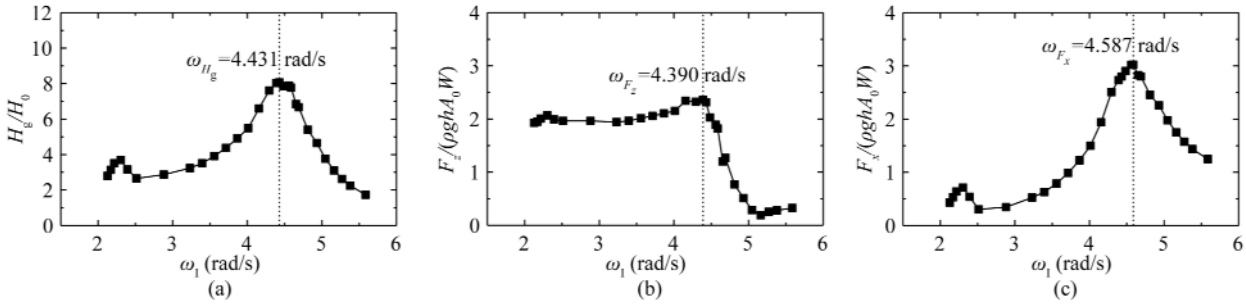

Fig. 2. Variations of (a) the total wave height in the gap, (b) the total vertical wave force, and (c) the total horizontal wave force with respect to the incident wave frequency, ω_I, for H_0=0.024 m and S=0.050.

as the fluid resonant frequency. In Fig. 2b, the wave frequency that corresponds to the maximum vertical wave force, ω_{Fz}, deviates from the fluid resonant frequency and is called the vertical-force resonant frequency. Similarly, the symbol ω_{Fx} in Fig. 2c is referred to as the horizontal-force resonant frequency, and it is also different from the fluid resonant frequency. Besides, the values of ω_F and ω_{Fx} are shown to be different from each other.

Furthermore, because the lower limit of the incident wave frequency considered in this article significantly declines when compared with that in Gao et al. (2019a, 2020b), the 2nd-order gap resonance phenomenon is also observed in this figure. Specifically speaking, obvious secondary peaks appear around half of ω_{Hg} for all the three parameters. These secondary peaks are triggered by the 2nd-order harmonic component of the incident low-frequency waves, which will be elaborated in Subsections 4.2−4.4. It should be stressed that all these phenomena shown in Fig. 2 can also be observed for other sets of incident wave height and topographic slope.

4.2 Harmonic analyses of wave height inside the gap

Fig. 3 presents the ratios of the 2nd- to the 1st-order wave heights inside the gap for all cases under conditions of S=0, 0.050, 0.100, and 0.113. $H_g^{(1)}$ and $H_g^{(2)}$ denote the 1st- and the 2nd-order wave heights inside the gap, respectively. The fluid resonant frequencies for all the sets of the incident wave height and the topographic slope are also presented in this figure to better illustrate the relationship between the fluid resonance inside the gap and the values of $H_g^{(2)}/H_g^{(1)}$. Three apparent phenomena can be observed. Firstly, there generally exists a local maximum point of $H_g^{(2)}/H_g^{(1)}$ exactly at or very close to the fluid resonant frequency, except for the sets of S=0.113 and $H_0 \geqslant 0.075$ m in which there is an obvious deviation between the frequency corresponding to the local maximum point and the fluid res-

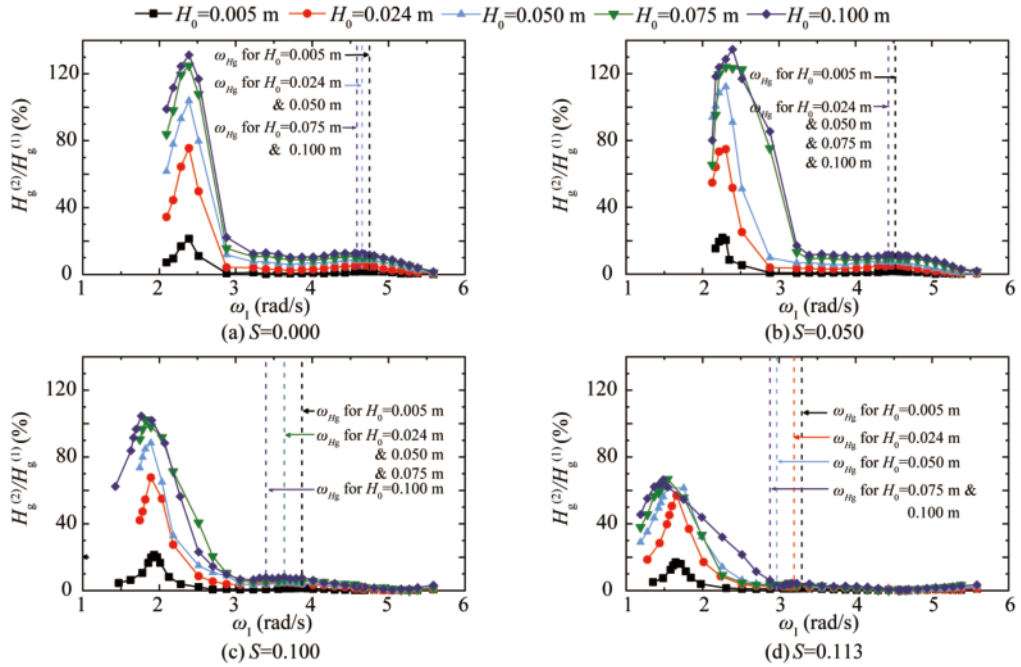

Fig. 3. Ratios of the 2nd- to the 1st-order wave heights inside the gap for all cases under conditions of S=0, 0.050, 0.100, and 0.113. $H_g^{(1)}$ and $H_g^{(2)}$ denote the 1st- and the 2nd-order wave heights in the gap, respectively.

onant frequency. Secondly, for all the topographies, the value of $H_g^{(2)}/H_g^{(1)}$ appears to increase with the increase of H_0 at almost the whole range of the incident wave frequency considered.

Thirdly, apart from the local maximum point near the fluid resonant frequency, there exists a maximum value of $H_g^{(2)}/H_g^{(1)}$ at the low-frequency range (i.e., ω_1<2.8 rad/s). Further examining the wave frequency corresponding to the maximum value of $H_g^{(2)}/H_g^{(1)}$, one can find that it is always approximately equal to half of the fluid resonant frequency for each set of incident wave height and topographic slope. In addition, the maximum value of $H_g^{(2)}/H_g^{(1)}$ at the low-frequency range is shown to be much larger than that near the fluid resonant frequency. The former can even exceed 100% for larger incident wave heights, while the latter is always less than 20%. It proves that the occurrence of the 2nd-order gap resonance phenomenon is triggered by the 2nd-order harmonic components of the incident low-frequency waves. It is noted here that the three phenomena mentioned above can also be observed for the other two slopes with S=0.025 and 0.075 (the detailed results for these two slopes are not presented due to space limitation).

Fig. 4 shows the ratios of the 3rd- to the 1st-order wave heights inside the gap for all the cases shown in Fig. 3. $H_g^{(3)}$ in the figure denotes the 3rd-order wave heights in the gap. The three phenomena shown in Fig. 3 can also be easily observed in this figure, except that the values of $H_g^{(3)}/H_g^{(1)}$ are much smaller than the corresponding ones of $H_g^{(2)}/H_g^{(1)}$.

To visually show the nonlinear characteristics of the resonant wave heights and the effects of the incident wave heights on them, Fig. 5 illustrates the variations of $H_g^{(2)}/H_g^{(1)}$ and $H_g^{(3)}/H_g^{(1)}$ at the fluid resonant frequency

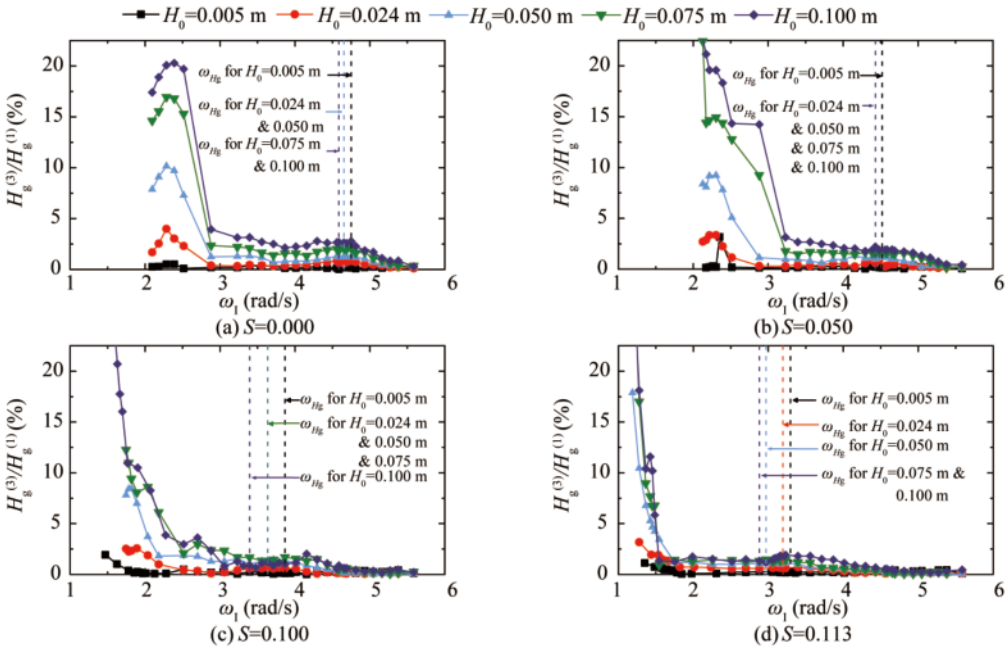

Fig. 4. Ratios of the 3rd- to the 1st-order wave heights inside the gap for all cases, in which $H_g^{(3)}$ denotes the 3rd-order wave heights in the gap.

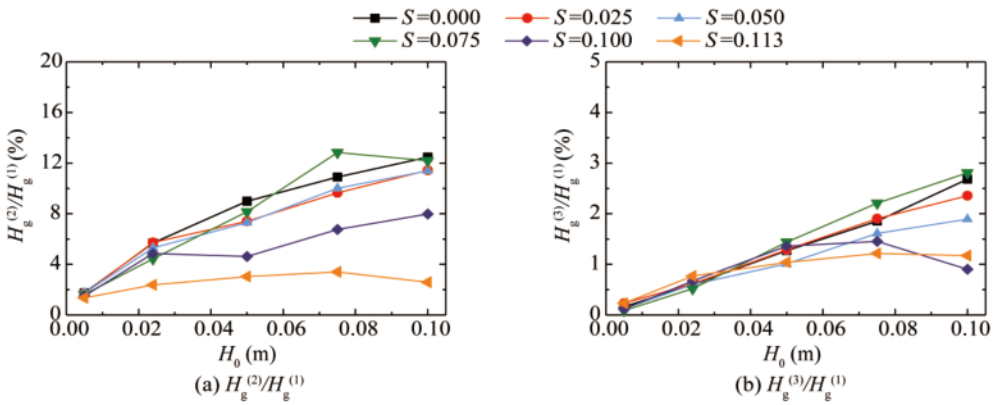

Fig. 5. Variations of (a) $H_g^{(2)}/H_g^{(1)}$ and (b) $H_g^{(3)}/H_g^{(1)}$ at the fluid resonant frequency with respect to the incident wave height, H_0, for all the topographic slopes.

with respect to the incident wave height, H_0, for all the topographic slopes. For both $H_g^{(2)}/H_g^{(1)}$ and $H_g^{(3)}/H_g^{(1)}$ at the fluid resonant frequency, their values increase gradually with the incident wave heights overall. The maximum values of $H_g^{(2)}/H_g^{(1)}$ and $H_g^{(3)}/H_g^{(1)}$ at the fluid resonant frequency are equal to 12.8% and 2.8%, respectively.

To reveal the influence of the topographic slope on the nonlinearity of the resonant wave height, Fig. 6 presents the variations of $H_g^{(2)}/H_g^{(1)}$ and $H_g^{(3)}/H_g^{(1)}$ at the fluid resonant frequency with respect to the topographic slope for all the incident wave heights. Two apparent phenomena can be observed. Firstly, for both $H_g^{(2)}/H_g^{(1)}$ and $H_g^{(3)}/H_g^{(1)}$, the influencing degree of the slope on them seems to depend closely on the incident wave height, H_0. In general, the smaller the incident wave height is, the lower the influencing degree of the slope becomes. Secondly, when the box-wall system is subjected to the incident waves with larger wave heights, larger topographic slopes (S>0.075) can remarkably inhibit the high-order components (including the 2nd- and the 3rd-order ones).

4.3 Harmonic analyses of vertical wave forces

Fig. 7 presents the ratios of the high-order to the 1st-order vertical wave forces under conditions of S=0 and 0.100, in which $F_z^{(m)}$ (m=1, 2 and 3) denotes the mth-order vertical wave force. For the topography with S=0 (Figs. 7a and 7c), the values of both $F_z^{(2)}/F_z^{(1)}$ and $F_z^{(3)}/F_z^{(1)}$ are shown to first increase and then decrease with the wave frequency at the frequency range of ω_I>3.0 rad/s. For each set of S and H_0, there exists a maximum point for both $F_z^{(2)}/F_z^{(1)}$ and $F_z^{(3)}/F_z^{(1)}$ at a certain frequency that is significantly larger than the vertical-force resonant frequency, ω_{F_z}. In addition,

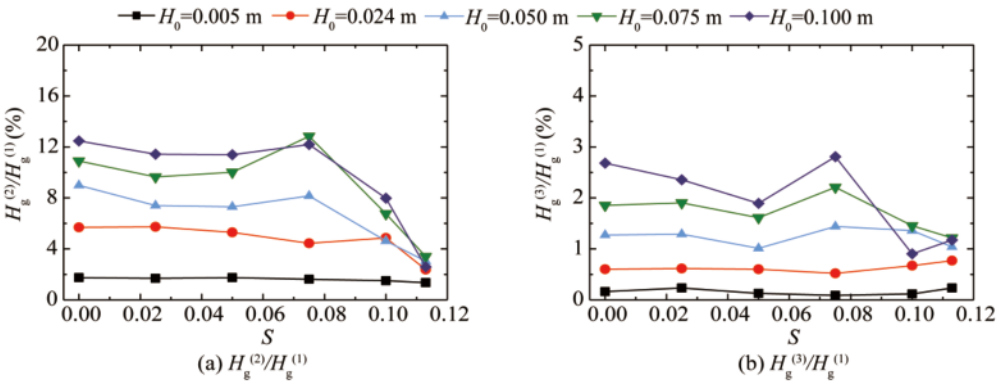

Fig. 6. Variations of (a) $H_g^{(2)}/H_g^{(1)}$ and (b) $H_g^{(3)}/H_g^{(1)}$ at the fluid resonant frequency with respect to the topographic slope for all the incident wave heights.

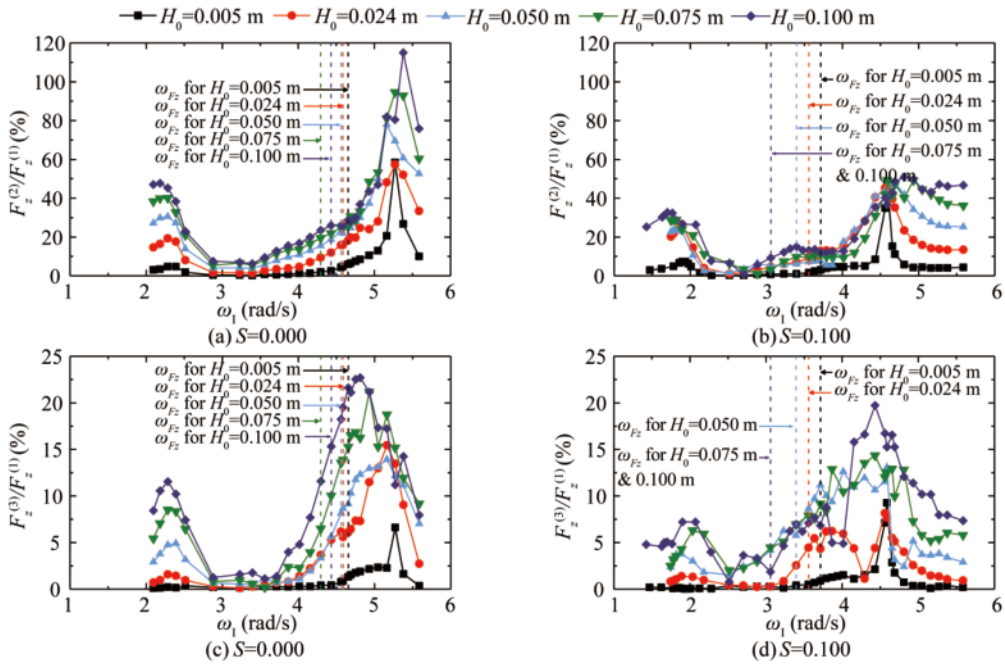

Fig. 7. Ratios of the high-order to the 1st-order vertical wave forces under conditions of S=0 and 0.100. (a) and (b) correspond to the ratios of the 2nd- to the 1st-order ones, and (c) and (d) correspond to the ratios of the 3rd- to the 1st-order ones. $F_z^{(m)}$ (m=1, 2 and 3) denote the mth-order vertical wave force.

for each set of S and H_0, the values of both $F_z^{(2)}/F_z^{(1)}$ and $F_z^{(3)}/F_z^{(1)}$ at the vertical-force resonant frequency appear to be remarkably less than their corresponding maximum values. In addition, at the low-frequency range (i.e., ω_I<2.8 rad/s), there always exist secondary peaks for both $F_z^{(2)}/F_z^{(1)}$ and $F_z^{(3)}/F_z^{(1)}$ due to the occurrence of the 2nd-order gap resonance. For the topography with S=0.100 (Figs. 7b and 7d), the variation trends of both $F_z^{(2)}/F_z^{(1)}$ and $F_z^{(3)}/F_z^{(1)}$ are similar to those for the topography with S=0 overall. It should be noted that all these phenomena for S=0 and 0.100 can also be observed for the other four slopes (i.e., S=0.025, 0.050, 0.075, and 0.113). In what follows, the influences of the incident wave height and the topographic slope on the values of $F_z^{(2)}/F_z^{(1)}$ and $F_z^{(3)}/F_z^{(1)}$ at the vertical-force resonant frequency, ω_{F_z}, and on their maximum values are discussed one by one in detail.

Fig. 8 illustrates the variations of the ratios of the high-order vertical wave forces at ω_{F_z} and the maximum ratios with respect to H_0 for all the topographic slopes. Three obvious phenomena can be observed. Firstly, in general, the relative importance of the high-order vertical wave forces to the 1st-order components becomes more and more evident with the increase of the incident wave height, no matter for the ratios at ω_{F_z} (Figs. 8a and 8b), or for the maximum ones (Figs. 8c and 8d). Secondly, the maximum value of $F_z^{(2)}/F_z^{(1)}$ for each set of S and H_0 is significantly larger than the corresponding ratio at ω_{F_z}. Among all the sets of S and H_0, the maximum value of $F_z^{(2)}/F_z^{(1)}$ can approach 120% (Fig. 8c), while the value of $F_z^{(2)}/F_z^{(1)}$ at ω_{F_z} is always smaller than 30% (Fig. 8a). It indicates that although the maximum value of the total vertical wave force appears at ω_{F_z}, $F_z^{(2)}/F_z^{(1)}$ at that frequency is far less than the maximum $F_z^{(2)}/F_z^{(1)}$ which appears at a much higher frequency than ω_{F_z}. Thirdly, for the largest two slopes (i.e., S=0.100 and 0.113), in general, the ratios of the high-order vertical force seem less than those for the other four slopes in the variation range of H_0 considered. This indicates that the much larger slope would effectively restrain the relative importance of the high-order vertical forces to the 1st-order ones, which is similar to the corresponding phenomenon for the wave height inside the gap shown in Fig. 6.

Fig. 9 further illustrates the variations of the ratios of the high-order vertical wave forces with respect to S for all the incident wave heights. The third phenomenon described above can also be visually observed from this figure.

4.4 Harmonic analyses of horizontal wave forces

Fig. 10 presents the ratios of the high-order to the 1st-order horizontal wave forces under conditions of S=0 and 0.100, in which $F_x^{(m)}$ (m=1, 2 and 3) denote the mth-order horizontal wave force. For all $F_x^{(2)}/F_x^{(1)}$ in each set of S and H_0 (Figs. 10a and 10b), their maximum values always occur at the low-frequency range, and as the wave frequency increases, the value of $F_x^{(2)}/F_x^{(1)}$ gradually decreases. At the horizontal-force resonant frequency, ω_{F_x}, the ratio for $F_x^{(2)}/F_x^{(1)}$ has dropped to a reasonably small value. Take the

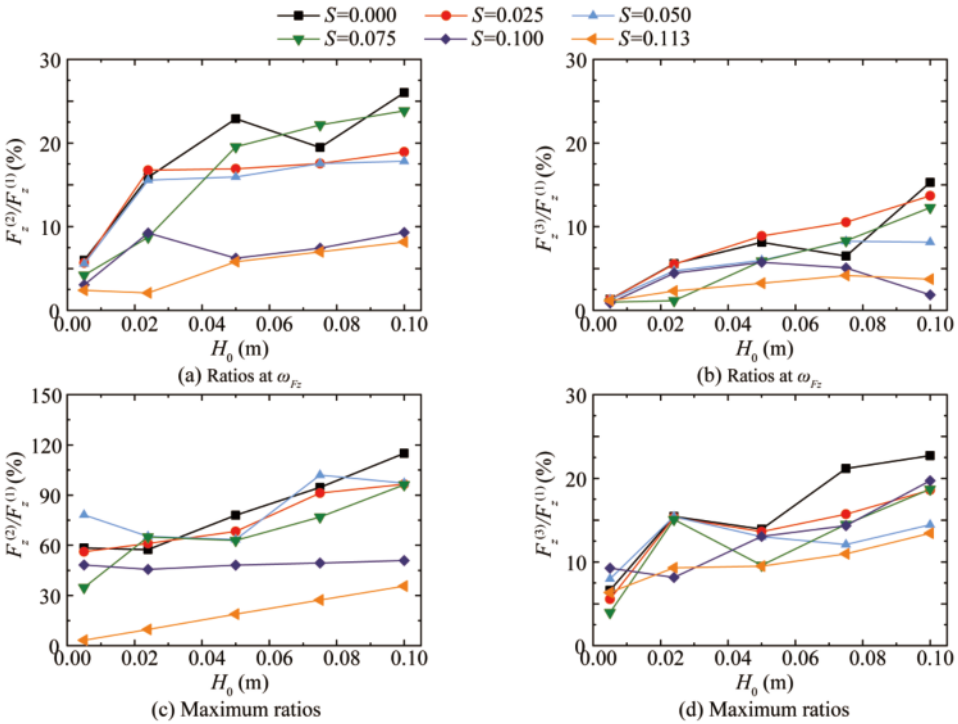

Fig. 8. Variations of the ratios of the high-order vertical wave forces at ω_{F_z} and their maximum ratios with respect to H_0 for all the topographic slopes. (a) and (b) correspond to $F_z^{(2)}/F_z^{(1)}$ and $F_z^{(3)}/F_z^{(1)}$ at ω_{F_z}, respectively; (c) and (d) correspond to the maximum $F_z^{(2)}/F_z^{(1)}$ and the maximum $F_z^{(3)}/F_z^{(1)}$ for a specific set of S and H_0, respectively.

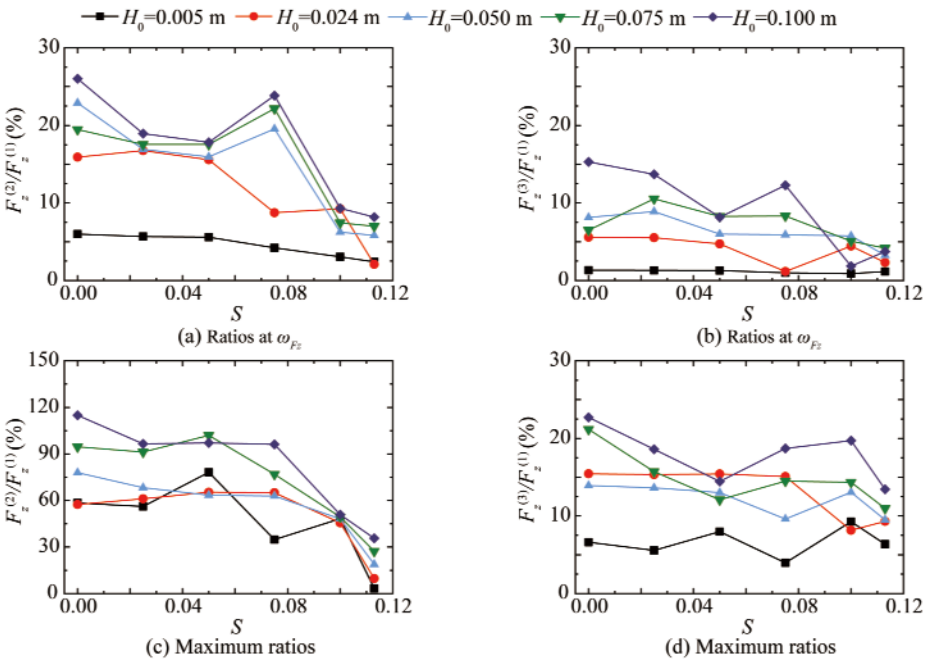

Fig. 9. As in Fig. 8, but for the variations of the ratios of the high-order vertical wave forces with respect to *S* for all the incident wave heights.

set of S=0 and H_0=0.100 m for example (see Fig. 10a), the maximum $F_x^{(2)}/F_x^{(1)}$ exceeds 300% at ω_I =2.514 rad/s due to the occurrence of the 2nd-order gap resonance, while the value of $F_x^{(2)}/F_x^{(1)}$ at ω_{F_x}=4.812 rad/s is only 3.84%. For the ratios of $F_x^{(3)}$ to $F_x^{(1)}$ (Figs. 10c and 10d), the maximum value also appears at the low-frequency range. It is noted that the phenomena for the other four slopes (i.e., S=0.025, 0.050, 0.075 and 0.113) are very similar to those for S=0 and 0.100, and hence are not presented here.

Fig. 11 illustrates the variations of the ratios of the high-order horizontal wave forces at ω_{F_x} with respect to the incident wave height H_0 and the topographic slope S. For the effect of the incident wave height, it is seen that both $F_x^{(2)}/F_x^{(1)}$ and $F_x^{(3)}/F_x^{(1)}$ at ω_{F_x} increase gradually with the increase of H_0 overall (Figs. 11a and 11b). The maximum values of $F_x^{(2)}/F_x^{(1)}$ and $F_x^{(3)}/F_x^{(1)}$ at ω_{F_x} are equal to 14.4% and 4.6%, respectively. However, the topographic slope has different influencing features for different types of ratios.

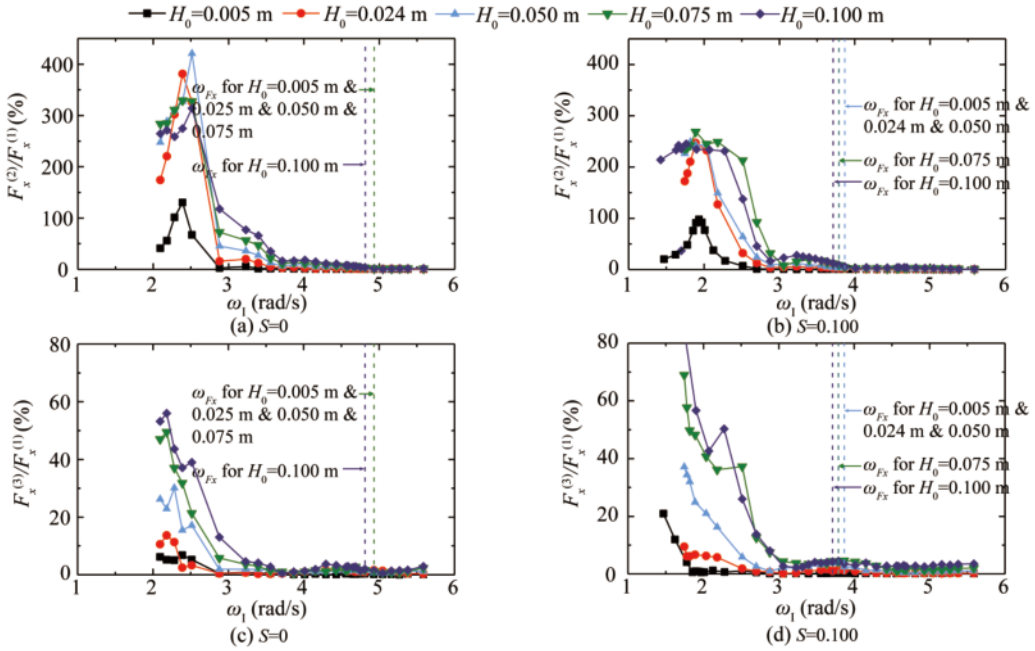

Fig. 10. Ratios of the high-order to the 1st-order horizontal wave forces under conditions of S=0 and 0.100. (a)−(b) correspond to the ratios of the 2nd- to the 1st-order ones, and (c)−(d) correspond to the ratios of the 3rd- to the 1st-order ones. $F_x^{(m)}$ (m=1, 2 and 3) denotes the mth-order horizontal wave force.

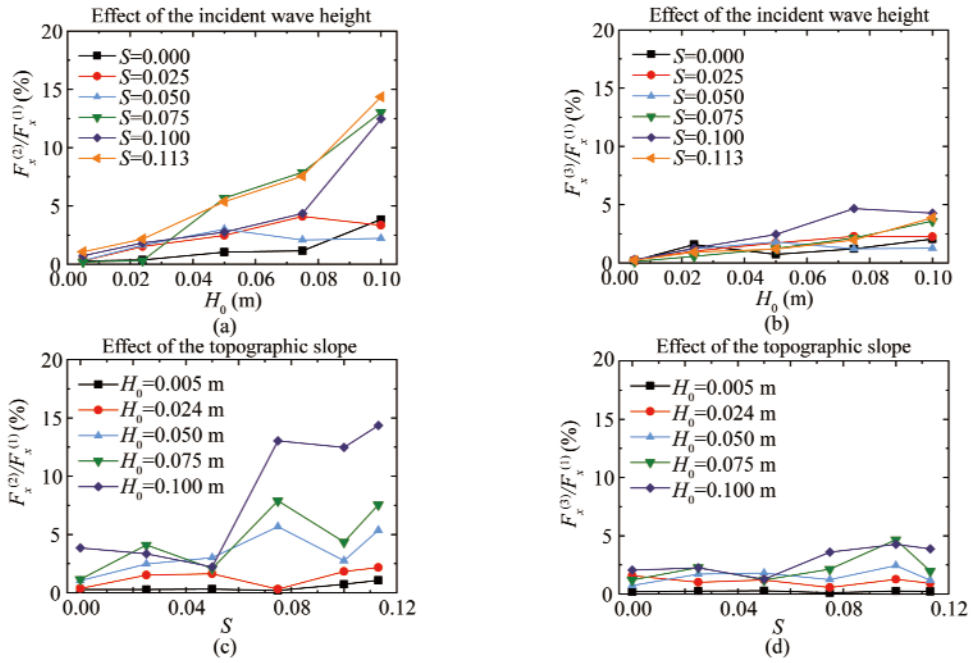

Fig. 11. Variations of both $F_x^{(2)}/F_x^{(1)}$ and $F_x^{(3)}/F_x^{(1)}$ at ω_{Fx} with respect to the incident wave height H_0 (a and b) and to the topographic slope S (c and d).

Specifically speaking, for $F_x^{(2)}/F_x^{(1)}$ at ω_{F_x}, their values rise gradually with the slope, although there exist fluctuations in the rising trend (Fig. 11c). While for $F_x^{(3)}/F_x^{(1)}$ at ω_{F_x}, their values are always shown to fluctuate around certain values (Fig. 11d). In addition, there are always different degrees of decline for them as S increases from 0.100 to 0.113.

4.5 Comparisons of harmonic analysis results

Based on the results given in Subsections 4.2−4.4, it is seen that for all the three parameters (i.e., the wave height inside the gap, the vertical wave force, and the horizontal wave force on the box) and all the sets of S and H_0 considered, the ratios of the high- to the 1st-order components at their respective resonant frequencies (i.e., ω_{H_g}, ω_{F_z}, and ω_{F_x}) are generally not the maximum ones. On the contrary, their maximum ratios usually appear at the wave frequencies that are either much higher or notably lower than their respective resonant frequencies. It means that the cases possessing the largest ratios of the high- to the 1st-order components correspond to relatively lower total wave height inside the gap and total wave loads on the box. In other words, these cases have moderately lower risks for the green water on the deck and the structural damage due to excessive loads. Hence, only the comparisons of the ratios at their respective resonant frequencies are carried out in this subsection.

Figs. 12 and 13 respectively present the comparisons between the ratios of both the 2nd- and the 3rd- to the 1st-order components for the three parameters at their resonant frequencies when H_0=0.005 m, 0.050 m and 0.100 m. It can be observed from Fig. 12 that among the three parameters, the values of $F_x^{(2)}/F_x^{(1)}$ at ω_{F_x} are usually minimal, and the values of $H_g^{(2)}/H_g^{(1)}$ at ω_{H_g} are often larger than the former but are always smaller than those of $F_z^{(2)}/F_z^{(1)}$ at ω_{F_z}. While for the ratios of the 3rd- to the 1st-order components shown in Fig. 13, $H_g^{(3)}/H_g^{(1)}$ at ω_{H_g} and $F_x^{(3)}/F_x^{(1)}$ at ω_{F_x} for all the sets of S and H_0 are shown to be very close to each other. In addition, similar to the ratios of the 2nd- to the 1st-order magnitudes, both $H_g^{(3)}/H_g^{(1)}$ and $F_x^{(3)}/F_x^{(1)}$ are also signific-

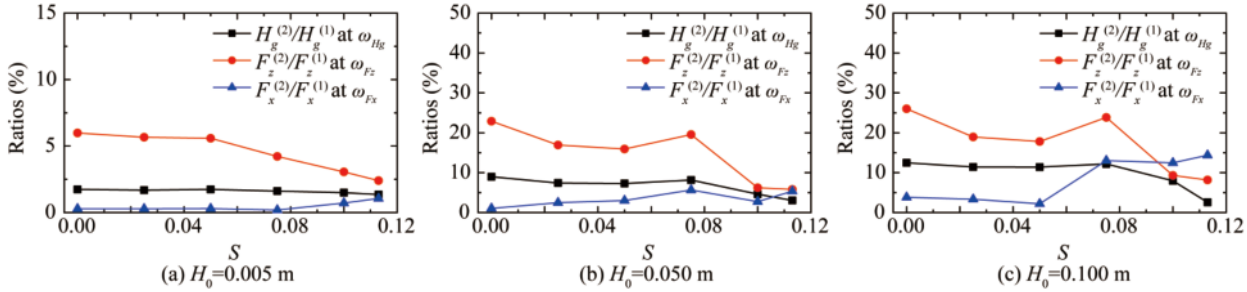

Fig. 12. Comparisons between the ratios of the 2nd- to the 1st-order components for wave heights in the gap and wave loads on the box at their respective resonant frequencies under conditions of H_0=0.005 m, 0.050 m and 0.100 m.

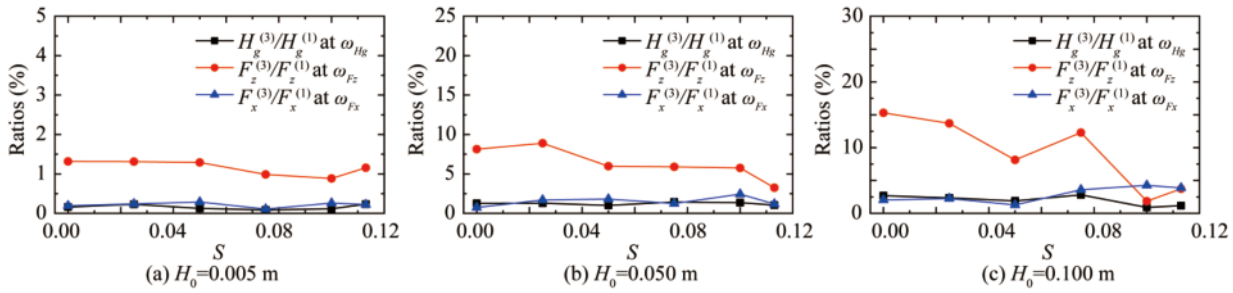

Fig. 13. As in Fig. 12, but for the ratios of the 3rd- to the 1st-order components.

antly smaller than $F_z^{(3)}/F_z^{(1)}$ at ω_{F_z}. Therefore, in practical engineering problems, enough attention should be paid to the contributions of the high-order components for the vertical wave force. It should be noted that the phenomena for the other two incident wave heights (i.e., H_0=0.024 m and 0.075 m) are very similar to those shown in those two figures, and hence are not presented here.

5 Conclusions

The focus of this paper is on the harmonic analyses of related hydrodynamic parameters during the gap resonance between a fixed box and a vertical wall excited by incident regular waves with various wave heights. The hydrodynamic parameters considered include the wave height inside the gap, the vertical wave force, and the horizontal wave force acting on the box. The local seabed in front of the vertical wall has variable topographic slopes. The viscous-flow numerical model, OpenFOAM®, combined with the "*waves2Foam*" toolbox is utilized to carry out the present investigations. The influences of the incident wave height and the topographic slope on the ratios of the high-order (including the 2nd- and the 3rd-order) to the 1st-order components for the three hydrodynamic parameters are systematically investigated. The research results of this article have provided new insights into the nonlinear characteristics of the hydrodynamic parameters involved in the gap resonance phenomenon formed by vessels berthing in front of wharfs.

The following main conclusions can be drawn from the present study:

(1) For the wave height inside the gap, there usually exists a maximum value of $H_g^{(2)}/H_g^{(1)}$ at the low-frequency range (i.e., ω_I<2.8 rad/s). Apart from the maximum point in the lower frequency range, there generally exists another local maximum point of $H_g^{(2)}/H_g^{(1)}$ exactly at or very close to the fluid resonant frequency. Similar phenomena can also be observed for $H_g^{(3)}/H_g^{(1)}$. For both $H_g^{(2)}/H_g^{(1)}$ and $H_g^{(3)}/H_g^{(1)}$ at the fluid resonant frequency, the relative importance of the high-order components increases gradually with the incident wave height overall. The topographic influence on them closely depends on the incident wave height.

(2) For the vertical and the horizontal wave forces, there also exists a maximum point for both the ratios of the 2nd- and the 3rd-order to the 1st-order components at a certain frequency which is significantly larger than (for the vertical wave force) or notably lower than (for the horizontal wave force) their respective resonant frequency. In addition, for each set of S and H_0, both the ratios of the 2nd- and the 3rd-order to the 1st-order components at the resonant frequency appear to be remarkably less than their corresponding maximum ratios. For both the 2nd- and the 3rd-order wave loads, their relative importance also increases gradually with the incident wave height. Meanwhile, the topographic influence on them depends heavily on the type of wave loads and the incident wave height.

(3) Among the three parameters, the values of $F_x^{(2)}/F_x^{(1)}$ at ω_{F_x} are usually minimal, and the values of $H_g^{(2)}/H_g^{(1)}$ at ω_{H_g} are often larger than the former but always smaller than those of $F_z^{(2)}/F_z^{(1)}$ at ω_{F_z}. $H_g^{(3)}/H_g^{(1)}$ at ω_{H_g} and $F_x^{(3)}/F_x^{(1)}$ at ω_{F_x} for all the sets of S and H_0 are very close to each other, and both are apparently less than $F_z^{(3)}/F_z^{(1)}$ at ω_{F_z} overall. Hence, in practical engineering, enough attention should be paid to the contributions of the high-order components for the vertical wave force on the box.

(4) When the frequency of the incident waves is approximately equal to half of the fluid resonant frequency, the significant 2nd-order gap resonance phenomenon is observed in the present study. Under this condition, the 2nd-order wave height and horizontal force can become significantly larger than the corresponding 1st-order components when the incident waves have larger wave heights.

Finally, we reaffirm that the above conclusions are only valid for the variation ranges of the topographic slope and the incident wave height considered in this paper and for the given geometric layout (including the size and draft of the box, the gap width, and the water depth).

References

Berberović, E., van Hinsberg, N.P., Jakirlić, S., Roisman, I.V. and Tropea, C., 2009. Drop impact onto a liquid layer of finite thickness: Dynamics of the cavity evolution, *Physical Review E*, 79(3), 036306.

Chen, L.F., Zang, J., Taylor, P.H., Sun, L., Morgan, G.C.J., Grice, J., Orszaghova, J. and Ruiz, M.T., 2018. An experimental decomposition of nonlinear forces on a surface-piercing column: Stokes-type expansions of the force harmonics, *Journal of Fluid Mechanics*,

848, 42–77.

Gao, J.L., Chen, H.Z., Zang, J., Chen, L.F., Wang, G. and Zhu, Y.Z., 2020a. Numerical investigations of gap resonance excited by focused transient wave groups, *Ocean Engineering*, 212, 107628.

Gao, J.L., He, Z.W., Huang, X.H., Liu, Q., Zang, J. and Wang, G., 2021a. Effects of free heave motion on wave resonance inside a narrow gap between two boxes under wave actions, *Ocean Engineering*, 224, 108753.

Gao, J.L., He, Z.W., Zang, J., Chen, Q., Ding, H.Y. and Wang, G., 2019a. Topographic effects on wave resonance in the narrow gap between fixed box and vertical wall, *Ocean Engineering*, 180, 97–107.

Gao, J.L., He, Z.W., Zang, J., Chen, Q., Ding, H.Y. and Wang, G., 2020b. Numerical investigations of wave loads on fixed box in front of vertical wall with a narrow gap under wave actions, *Ocean Engineering*, 206, 107323.

Gao, J.L., Ma, X.Z., Chen, H.Z., Zang, J. and Dong, G.H., 2021b. On hydrodynamic characteristics of transient harbor resonance excited by double solitary waves, *Ocean Engineering*, 219, 108345.

Gao, J.L., Ma, X.Z., Dong, G.H., Zang, J., Zhou, X.J. and Zhou, L., 2019b. Topographic influences on transient harbor oscillations excited by N-waves, *Ocean Engineering*, 192, 106548.

Gao, J.L., Ma, X.Z., Dong, G.H., Chen, H.Z., Liu, Q. and Zang, J., 2021c. Investigation on the effects of Bragg reflection on harbor oscillations, *Coastal Engineering*, 170, 103977.

Gao, J.L., Ma, X.Z., Zang, J., Dong, G.H., Ma, X.J., Zhu, Y.Z. and Zhou, L., 2020c. Numerical investigation of harbor oscillations induced by focused transient wave groups, *Coastal Engineering*, 158, 103670.

Gao, J.L., Zang, J., Chen, L.F., Chen, Q., Ding, H.Y. and Liu, Y.Y., 2019c. On hydrodynamic characteristics of gap resonance between two fixed bodies in close proximity, *Ocean Engineering*, 173, 28–44.

Gao, J.L., Zhou, X.J., Zhou, L., Zang, J. and Chen, H.Z., 2019d. Numerical investigation on effects of fringing reefs on low-frequency oscillations within a harbor, *Ocean Engineering*, 172, 86–95.

Grue, J. and Huseby, M., 2002. Higher-harmonic wave forces and ringing of vertical cylinders, *Applied Ocean Research*, 24(4), 203–214.

He, Z.W., Gao, J.L., Zang, J., Chen, H.Z., Liu, Q. and Wang, G., 2021. Effects of free heave motion on wave forces on two side-by-side boxes in close proximity under wave actions, *China Ocean Engineering*, 35(4), 490–503.

Jacobsen, N.G., Fuhrman, D.R. and Fredsøe, J., 2012. A wave generation toolbox for the open-source CFD library: OpenFoam®, *International Journal for Numerical Methods in Fluids*, 70(9), 1073–1088.

Jensen, B.L., Sumer, B.M. and Fredsøe, J., 1989. Turbulent oscillatory boundary layers at high Reynolds numbers, *Journal of Fluid Mechanics*, 206, 265–297.

Jiang, S.C., Bai, W., Cong, P.W. and Yan, B., 2019. Numerical investigation of wave forces on two side-by-side non-identical boxes in close proximity under wave actions, *Marine Structures*, 63, 16–44.

Li, B.N., Cheng, L., Deeks, A.J. and Teng, B., 2005. A modified scaled boundary finite-element method for problems with parallel side-faces. Part II. Application and evaluation, *Applied Ocean Research*, 27(4–5), 224–234.

Li, Y.J., 2019. Fully nonlinear analysis of second-order gap resonance between two floating barges, *Engineering Analysis with Boundary Elements*, 106, 1–19.

Liu, Y., Li, H.J., Lu, L., Li, A.J. and Tan, L., 2020. A semi-analytical potential solution for wave resonance in gap between floating box and vertical wall, *China Ocean Engineering*, 34(6), 747–759.

Lu, L., Tan, L., Zhou, Z.B., Zhao, M. and Ikoma, T., 2020. Two-dimensional numerical study of gap resonance coupling with motions of floating body moored close to a bottom-mounted wall, *Physics of Fluids*, 32(9), 092101.

Lu, L., Teng, B., Cheng, L., Sun, L. and Chen, X.B., 2011. Modelling of multi-bodies in close proximity under water waves—Fluid resonance in narrow gaps, *Science China Physics*, *Mechanics and Astronomy*, 54(1), 16–25.

Miao, G.P., Ishida, H. and Saitoh, T., 2000. Influence of gaps between multiple floating bodies on wave forces, *China Ocean Engineering*, 14(4), 407–422.

Miao, G.P., Saitoh, T. and Ishida, H., 2001. Water wave interaction of twin large scale caissons with a small gap between, *Coastal Engineering Journal*, 43(1), 39–58.

Molin, B., Remy, F., Kimmoun, O. and Stassen, Y., 2002. Experimental study of the wave propagation and decay in a channel through a rigid ice-sheet, *Applied Ocean Research*, 24(5), 247–260.

Moradi, N., Zhou, T.M. and Cheng, L., 2015. Effect of inlet configuration on wave resonance in the narrow gap of two fixed bodies in close proximity, *Ocean Engineering*, 103, 88–102.

Ning, D.Z., Zhu, Y., Zhang, C.W. and Zhao, M., 2018. Experimental and numerical study on wave response at the gap between two barges of different draughts, *Applied Ocean Research*, 77, 14–25.

Saitoh, T., Miao, G.P. and Ishida, H., 2006. Theoretical analysis on appearance condition of fluid resonance in a narrow gap between two modules of very large floating structure, *Proceedings of the 3rd Asia-Pacific Workshop on Marine Hydrodynamics*, Shanghai, China, pp. 170–175.

Sun, L., Taylor, R.E. and Taylor, P.H., 2010. First- and second-order analysis of resonant waves between adjacent barges, *Journal of Fluids and Structures*, 26(6), 954–978.

Tan, L., Lu, L., Liu, Y., Sabodash, O.A. and Teng, B., 2014. Dissipative effects of resonant waves in confined space formed by floating box in front of vertical wall, *Proceedings of the 11th ISOPE Pacific/Asia Offshore Mechanics Symposium*, Shanghai, China.

Tan, L., Lu, L., Tang, G.Q., Cheng, L. and Chen, X.B., 2019. A viscous damping model for piston mode resonance, *Journal of Fluid Mechanics*, 871, 510–533.

Tan, L., Lu, L., Tang, G.Q. and Cheng, L., 2020. A dynamic solution for predicting resonant frequency of piston mode fluid oscillation in moonpools/narrow gaps, *Journal of Hydrodynamics*, 32(1), 54–69.

Wang, H., Wolgamot, H.A., Draper, S., Zhao, W., Taylor, P.H. and Cheng, L., 2019. Resolving wave and laminar boundary layer scales for gap resonance problems, *Journal of Fluid Mechanics*, 866, 759–775.

Zhao, W., Milne, I.A., Efthymiou, M., Wolgamot, H.A., Draper, S., Taylor, P.H. and Taylor, R.E., 2018. Current practice and research directions in hydrodynamics for FLNG-side-by-side offloading, *Ocean Engineering*, 158, 99–110.

Zhao, W., Wolgamot, H.A., Taylor, P.H. and Taylor, R.E., 2017. Gap resonance and higher harmonics driven by focused transient wave groups, *Journal of Fluid Mechanics*, 812, 905–939.